A Fast Spectral Method for Active 3D Shape Reconstruction

Jia Li, Alfred O. Hero

Abstract

Variational energy minimization techniques for surface reconstruction are implemented by evolving an active surface according to the solutions of a sequence of elliptic partial differential equations (PDE's). For these techniques, most current approaches to solving the elliptic PDE are iterative involving the implementation of costly finite element methods (FEM) or finite difference methods (FDM). The heavy computational cost of these methods makes practical application to 3D surface reconstruction burdensome. In this paper, we develop a fast spectral method which is applied to 3D active surface reconstruction of star-shaped surfaces parameterized in polar coordinates. For this parameterization the Euler-Lagrange equation is a Helmholtz-type PDE governing a diffusion on the unit sphere. After linearization, we implement a spectral non-iterative solution of the Helmholtz equation by representing the active surface as a double Fourier series over angles in spherical coordinates. We show how this approach can be extended to include region-based penalization. A number of 3D examples and simulation results are presented to illustrate the performance of our fast spectral active surface algorithms.

Keywords

Star-shaped surfaces, active contour surface reconstruction, double Fourier series, spherical harmonics, Helmholtz equation.

I. INTRODUCTION

Partial differential equations (PDE's) have been widely applied to solve many computer vision and image processing problems, such as curvature based contour flow, edge-preserving image smoothing, image registration via deformable models, and image segmentation. The advantages of applying PDE methods to image analysis have been summarized in [7]. In particular, some of these problems, such as shape from shading [17], surface reconstruction [35] and active surfaces [12], can be formulated in the framework of energy minimization. Variational principles can be applied to find the energy minimizing surface and lead to solving partial differential equation (PDE) of elliptic type for the minimizing surface f

$$\nabla^2 f - \mu f = g, \tag{1}$$

where g is surface derived from the image data, e.g., a noisy edge map. Since direct solution of (1) can be quite difficult, one can perform successive approximations to (1) over time leading to a sequence of solutions $\{f_n\}_n$ called *active surfaces*. Methods which reconstruct surfaces by solving a sequence of PDE's are known as variational methods of energy minimization.

This paper is concerned with implementation of fast variational methods for the reconstruction of smooth star-shaped 3D surfaces. The majority of variational approaches to 3D object reconstruction solve PDE's on a rectangular domain, e.g. the plane $\Omega \in \mathbb{R}^2$. Such a 2D representation is natural as a 3D surface is simply a mapping $\mathbf{x} : \Omega \to \mathbb{R}^3$, i.e. $\mathbf{x}(v, w) = (x_1(v, w), x_2(v, w), x_3(v, w))$, where $(v, w) \in \Omega$. These approaches solve the obtained PDE's by iterative techniques, such as finite element methods (FEM) and finite difference methods (FDM). For example, in [10] Cohen used FEM to solve the PDE's in active balloons models and in [37] Xu used FDM to solve the PDE's for gradient vector flow. The advantage of FEM methods is their

J. Li is with the Department of Computer Science and Engineering, Oakland University, Rochester, MI, 48309 USA. E-mail: li4@oakland.edu

A. O. Hero is with the Department of Electrical Engineering and Computer Science, The University of Michigan, Ann Arbor, MI, 48109 USA. E-mail: hero@eecs.umich.edu

This work was supported in part by National Institutes of Health grants 1P01 CA87634-01 and R01 CA87955.

geometric flexibility due to their ability to perform local mesh refinement. However, FEM/FDM have met with difficulties for practical 3D imaging applications. The large number of voxels in 3D images causes significant growth of computation time which is intolerable in many practical applications.

This paper presents a method for accelerating active surface reconstruction for 3D star-shape objects. We adopt a polar version of the active balloon framework introduced by Cohen [10]. The surface functions of such objects and the associated PDE's can be defined over the unit sphere S^2 instead of a 2D rectangular domain, where $S^2 := \{(x, y, z) : x^2 + y^2 + z^2 = 1\}$ in the cartesian coordinate system or $S^2 := \{(r, \theta, \phi) : r = 1\}$ in the spherical coordinate system. With the assumption that the origin has been aligned with the object center, any star-shaped 3D surface can be naturally modelled by a single valued radial description function, $f(\theta, \phi) : S^2 \rightarrow \mathbb{R}$ defined on the unit sphere. Orthogonal functions on the unit sphere, such as spherical harmonics and double Fourier series have been widely used to decompose the radial descriptor f so that the statistical information on the corresponding coefficients can be used to guide other image processing tasks, such as deformation analysis [16] and image segmentation [32]. In fact, the radial descriptor f can be applied to the wide class of any simply connected (no hole) surface which can be embedded into the unit sphere. For example, in [6] Brechbühler proposed to parameterize the surfaces of simply connected 3D objects by defining a continuous, one-to-one mapping from the surface of the original object to the surface of a unit sphere. The parameterization is implemented via a constrained optimization procedure. In [34], Tao proposed to build a statistical shape model of cortical sulci by projecting sulci onto the unit sphere and extracting intersubject variability of the shape of the sulci and of the mean curvature along the sulcal curves.

PDE algorithms on the unit sphere have been widely studied for the numerical simulation of turbulence and phase transition, weather prediction and the study of ocean dynamics. In 1970's, spectral methods and pseudo-spectral methods on the unit sphere emerged as a viable alternative to finite difference and finite element methods [3], [4], [25]. It is well known that such spectral methods (SM) have unsurpassed accuracy for boundaryless periodic domains like the unit sphere and enjoy a faster rate of convergence than that of FDM and FEM for solving PDE's [15]. To further accelerate run-time without loss in accuracy, Cheong [9] and Yee [38] have devised less computationally demanding alternatives to the spherical harmonic basis. These results form our prime motivation for applying fast spectral methods to 3D surface reconstruction with degraded image-domain information, such as broken or blurred edge maps [19], [10].

Fourier snakes using spherical harmonic representations have been proposed for 3D deformable shape models by Staib and Duncan [31], and Székely *etal* [33]. The Mumford-Shah energy functional [24] was introduced by Chan to deal with blurred or broken boundary problem [8]. An alternative approach is to incorporate region-based grey-level information into the reconstruction process [18] and [36]. The work described in this paper combines and extends these approaches in several novel ways. First, we adopt a different total energy functional from [33] and [24] which accounts for an incomplete edge map by using a 3D Chamfer-like distance function [11] to enforce edge information, and an internal energy which combines a surface roughness penalty and a grey-scale region-based penalty similar to that used in [13] and [18]. Second, we adopt the variational approach of [10] to minimize the energy functional and we show that the Euler-Lagrange equations reduce to a non-linear PDE over the unit sphere describing the energy minimizing surface. Third, temporal evolution of the active surface is obtained directly by linearization of this PDE via successive approximations. This linearization leads to an evolving surface arising from successive solution of a sequence of homogeneous Helmholtz PDE's. Fourth, instead of spherical harmonics we apply the faster Cheong's double Fourier series [9] to solve each of these successive Helmholtz PDE's. These four attributes are the essence of our fast spectral methods (FSM).

This paper is organized as follows. In the next section, we briefly review the use of PDE's and variational principles for surface reconstruction via 3D active surfaces. In Section III we describe the general spectral method on the unit sphere proposed by Cheong. Simulation and experimental results are provided in Section IV. Finally in Section V we discuss current limitations of the methods and future research directions. The

reader interested in more details and additional applications of surface reconstruction. segmentation, and registration is referred to the thesis of the first author [22].

II. PDE'S IN SURFACE RECONSTRUCTION

A. Surface Reconstruction

Let $g = g(\theta, \phi)$ be a noisy radial function defiend in spherical coordinates (g, θ, ϕ). We call g the polar edge map and it is obtained from coarse segmentation of a star-shaped object. The surface reconstruction problem is to apply some form of regularization to approximate the rough edge map $g(\theta, \phi)$ by a smooth function $f(\theta, \phi)$. Variational approaches to this problem specify the solution f as a stationary point which minimizes the energy functional [12], [21]:

$$E(f, g) = \mu \int_{S^2} Y(f, g) d\Omega_{S^2} + \int_{S^2} Z(f) d\Omega_{S^2}, \tag{2}$$

where Y measures the distance between the function f and the polar edge map g, Z is a measure of reconstruction smoothness, μ controls the tradeoff between the faithfulness to the segmentation data and smoothness of the surface, and $d\Omega_{S^2}$ is a differential surface element on the unit sphere. The two terms on the right hand side of (2) represent the faithfulness to the segmentation data, called the data fidelity term, and the regularization penalty, called the smoothness term, respectively. If we define the data fidelity as the L_2 metric $Y(f, g) = (f(\theta, \phi) - g(\theta, \phi))^2$, the surface reconstruction problem $\min_f E(f, g)$ is equivalent to penalized least squares surface fitting. In order to enforce smoothness the term $Z(f)$ frequently contains the derivative of the function f. For instance, Z can be defined to be $Z(f) = \|\nabla f\|^2$, where ∇ is the gradient operator. With these choices, the energy functional becomes

$$E(f, g) = \int_{S^2} \mu (f(\theta, \phi) - g(\theta, \phi))^2 d\Omega_{S^2} + \int_{S^2} \|\nabla f(\theta, \phi)\|^2 d\Omega_{S^2}. \tag{3}$$

To minimize $E(f, g)$ over f one applies the calculus of variations [14] to determine an Euler-Lagrange equation for a stationary point of the above energy functional. This equation is

$$\nabla^2 f - \mu(f - g) = 0. \tag{4}$$

When specialized to spherical coordinates (4) becomes an elliptic equation of Helmholtz type [2], a fact that will be used in the sequel. When a time variable is included in the energy minimization functional (3) the elliptic equation becomes a function over both time and space. When indexed by the time variable the solutions to (4) are called an evolving surface or active surface.

Although FDM and FEM have been employed to solve the elliptic equation (4) they must be implemented iteratively at each time point. The FSM approach that will be introduced in Section III provide a non-iterative solution and therefore has lower computational complexity. In Section II-B and II-C, we will show that a non-linear PDE similar to (4) can be used to reconstruct 3D star-shaped surfaces with missing or broken edges. Due to the non-linearity of this PDE we will see that FSM must be implemented sequentially in time producing an evolving surface.

B. Parametric Active Surfaces on the Unit Sphere

Parametric active surface methods can be applied to simultaneously perform image segmentation and surface reconstruction. Let $\mathbf{x}$ be a general parametric description of a surface in $\mathbb{R}^3$, i.e., it is a mapping

$\mathbf{x} : \Omega \rightarrow \mathbb{R}^3$, where Ω is a subset of $\mathbb{R}^2$. We can represent a propagating surface as a parametric active surface $\mathbf{x}$ which minimizes the associated energy functional E,

$$E(\mathbf{x}) = \int_{\Omega} \left(P_{\text{ext}}(\mathbf{x}) + [\alpha \|\nabla \mathbf{x}\|^2 + \beta \|\nabla^2 \mathbf{x}\|^2] \right) d\Omega \tag{5}$$

where α and β are parameters controlling the smoothness of $\mathbf{x}$ and P_{ext} represents a potential function, e.g. the first term in the right side of (2). The term $\int_{\Omega} \alpha \|\nabla \mathbf{x}\|^2 + \beta \|\nabla^2 \mathbf{x}\|^2 d\Omega$, which does not depend on the data g extracted from the image, is called internal energy. The term $\int_{\Omega} P_{ext}(\mathbf{x}) d\Omega$, which is computed from the image data and the parametric surface $\mathbf{x}$, is called the external energy. The force generated by the internal energy discourages excessive stretching and bending of the surface. By suitably designing the function $P_{\text{ext}}(\mathbf{x})$, the force generated by the external energy can attract the surface towards extracted features of object, e.g. the edge map or grey level map. The surface $\mathbf{x}$ deforms under these two kinds of forces and converges to a minimizer of the energy functional E. Note that, as compared to (2), the representation (5) of the energy function is in a more standard form involving regularization parameters α and β which multiply the two surface roughness penalties.

The external force plays an important role in active surface methods. Typically, active surfaces are drawn towards the desired boundary by the external force which could include one or more of the following components: a traditional potential force, obtained by computing the negative gradient of an attraction potential defined over the image domain [12], [19]; a pressure force, used by Cohen in his balloon model [12], which could be either expanding or contracting depending on whether the surface is initialized from inside or outside of the obect; or a gradient vector flow, used by Xu [37] and obtained by diffusion of gradient of the edge-map. The role of the external force is to impose sufficient boundary information to extend the capture range to the initial surface.

Let $I : \mathbb{R}^3 \rightarrow \mathbb{R}$ represent the grey scale image volume to be segmented, $g := \{x_g, y_g, z_g\}$ be the set of all edge points detected in I which we call an edge map, and $d(g, (x, y, z))$ be the distance from a point (x, y, z) in the evolving surface $\mathbf{x}$ to the nearest edge point. Specifically, d can be written:. $d(g, (x, y, z)) \triangleq \min_{(x_g, y_g, z_g) \in g} \|(x, y, z) - (x_g, y_g, z_g)\|$. Figure 1 illustrates these relations. Potential functions designed to ensure fidelity to the edge map usually have a global minimum at the object boundary. Two common types of potential functions are:

$$P_{(1)}(\mathbf{x}) = h_1(\nabla I(\mathbf{x})), \tag{6}$$

$$P_{(2)}(\mathbf{x}) = h_2(d(g, \mathbf{x})), \tag{7}$$

where h_1 and h_2 are functions making $P_{(1)}$ and $P_{(2)}$ convex at the location of object boundary. For instance, $P(x, y, z) = -|\nabla I(x, y, z)|^2$, $P(x, y, z) = -|\nabla G_\sigma(x, y, z) * I(x, y, z)|^2$ and $P(x, y, z) = \frac{1}{1+|\nabla I|^p}$ belong to the type of $P_{(1)}$ [1]. In fact, $|\nabla I|$ serves as an edge detector which locates sharp intensity changes in image I. Potential functions of the type $P_{(1)}$ have the disadvantage that the resulting external force has very small capture range because $P_{(1)} \approx 0$ in homogeneous intensity areas. Potential functions of type $P_{(2)}$ increase the capture range by attracting the surface to the edge points, e.g. extracted by local edge detectors. Some common choices of $P_{(2)}$ are $P(x, y, z) = d^2(g, (x, y, z))$, $P(x, y, z) = \frac{-1}{d(g,(x,y,z))}$ and $P(x, y, z) = -e^{-d^2(g,(x,y,z))}$ [1]. In our experiment, we chose $d^2(g, \mathbf{x})$, a $P_{(2)}$-type potential function, to generate the external force for the active surface. This external force will make the active surface evolve towards the boundary along a path of minimal distance.

In (5), $\alpha \|\nabla \mathbf{x}\|^2$ and $\beta \|\nabla^2 \mathbf{x}\|^2$ separately control the active surface's elasticity and rigidity. The regularization effect coming from $\alpha \|\nabla \mathbf{x}\|^2$ can be interpreted as imposing a curvature based flow which has attractive geometric smoothing properties [20], [26]. A theorem in differential geometry states that any simple closed curve moving under its curvature collapses to a circle and then disappears [28]. Increasing α makes the active surface resistive to stretching, and introduces an intrinsic bias toward solutions that reduce the surface area.

On the other hand, increasing β makes the active surface more resistant to tensile stress and bending. To allow second-order discontinuity in the active surface, we set $\beta = 0$. The equation (5) is then reduced to

$$E(\mathbf{x}) = \int_{\Omega} \alpha \|\nabla \mathbf{x}\|^2 + d^2(g, \mathbf{x}) d\Omega. \tag{8}$$

For star-shaped surfaces the parameterization is most naturally expressed in an object-centered spherical coordinate system. As we will see, this representation permits computational acceleration by application of spectral methods. When there are missing or broken edges the edge map g is not specified for all angles θ, ϕ and the data fidelity term in (8) cannot be directly implemented. To deal with this we follow a similar procedure to that of Cohen *etal* [11] and use a Chamfer-like distance function to compute the data fidelity term. Specifically, we define a modified data fidelity term as

$$d(g, \mathbf{x}) = d(g, f) = \|f(\theta, \phi) - g_f(\theta, \phi)\|, \tag{9}$$

where $g_f(\theta, \phi)$ is defined as the point in the edge map g which is closest to the point $f(\theta, \phi)$ on the evolving surface

$$g_f(\theta, \phi) \triangleq \left\| \underset{(x_g, y_g, z_g) \in g}{\arg\min} \|(x_g, y_g, z_g) - f(\theta, \phi)(\sin\theta\cos\phi, \sin\theta\sin\phi, \cos\theta)\| - (x_o, y_o, z_o) \right\|, \tag{10}$$

and (x_o, y_o, z_o) represents the coordinates of the object center which is assumed known. The function g_f will be referred to as the closest edge map. (see Figure 1).

Equation (8) can now be rewritten as:

$$E(f) = \int_{S^2} \alpha \|\nabla f\|^2 + (f - g_f)^2 d\Omega_{S^2}. \tag{11}$$

Although equation (11) is analogous to equation (3), its associated Euler-Lagrange equation is not the same as (4). Since g_f is a non-linear function of f, the calculus of variations leads to a more complicated Euler-Lagrange equation:

$$\alpha \nabla^2 f - f = -(f - g_f)\frac{\partial g_f}{\partial f} - g_f, \tag{12}$$

where $\partial g_f / \partial f$ is a suitably defined variational of the closest edge map as a function of the evolving surface. While it would be worthwhile to explore conditions for existence of this variational we will sidestep this issue by making the approximation $|(f - g_f)\frac{\partial g_f}{\partial f}| \ll g_f$ in (12). This approximation can be justified in cases that the edge surface g_f encloses a large region and that f is close to g_f. To apply FSM in Section II-D, the elliptic PDE (12) will have to be linearized so that it becomes a homogeneous Helmholtz-type PDE.

C. Region-based Penalization

Traditional parametric and geometric active surfaces solely rely on the local edge detector to slow surface propagation. These methods do not use any region-based or volume-based information in the image. Such active surfaces can only segment and reconstruct objects whose boundaries are well defined, e.g. by the magnitude gradient $|\nabla I|$ of the image. For objects with blurred or broken boundaries, traditional active surfaces may extrude through holes in boundary. In [8] Chan proposed to use a Mumford-Shah energy functional [24] to deal with this "boundary leakage" problem. Other approaches [18] and [36] explicitly include region-based information into the segmentation. We use the same method as in [8] to incorporate the region-based information into the energy functional of 3D parametric active surface. The region-based

information is introduced as an additional penalty function. Define a new external energy functional $E_{\text{vol}}(f)$ associated with f as:

$$\begin{aligned} E_{\text{vol}}(f) &= \gamma\left(\int_{\text{inside}(f)}(I-u_{\text{in}})^2dV+\int_{\text{outside}(f)}(I-u_{\text{out}})^2dV\right) \\ &= \gamma\left(\int_{S^2}\left(\int_{r=0}^{f(\theta,\phi)}(I-u_{\text{in}})^2r^2dr+\int_{f(\theta,\phi)}^{B(I)}(I-u_{\text{out}})^2r^2dr\right)d\Omega_{S^2}\right), \end{aligned} \tag{13}$$

where $I = I(r,\theta,\phi)$ is the gray level intensity of the 3D image, $B(I)$ represents the boundary (assumed spherical for simplicity) of the image volume, and u_{in} and u_{out} are the mean intensities in the interior of the evolving surface f and outside f respectively.

$$u_{\text{in}} = \frac{\int_{\text{inside}(f)} IdV}{\text{vol}(\text{inside}(f))}, \qquad u_{\text{out}} = \frac{\int_{\text{outside}(f)} IdV}{\text{vol}(\text{outside}(f))}. \tag{14}$$

Here the denominators in (14) are the volumes inside and outside the evolving surface. With the assumption that the image intensity is nearly homogeneous inside and outside the object boundary, the new external energy functional (13) has the same minimizer as (11), which is the surface of the object. The functional (13)can be adjoined to the Lagrangian (11) by aggregating the integrals over S^2:

$$\begin{aligned} E(f,g) &= \int_{S^2}\Big\{\alpha\|\nabla f\|^2+(f-g_f)^2+ \\ &\quad \gamma\Big[\int_0^f(I-u_{\text{in}})^2r^2dr+\int_f^{B(I)}(I-u_{\text{out}})^2r^2dr\Big]\Big\}d\Omega_{S^2} \end{aligned} \tag{15}$$

which is called the region-penalized energy functional.

Next calculus of variations is applied to obtain the necessary condition for minimization of this penalized Lagrangian

$$\alpha\nabla^2 f-(f-g_f)(1-\frac{\partial g_f}{\partial f})-\gamma z(f,I)=0, \tag{16}$$

where

$$\begin{aligned} z(f,I) &= f^2\cdot[(I(f)-u_{\text{in}})^2-(I(f)-u_{\text{out}})^2]+2(\frac{\delta u_{\text{in}}}{\delta f})\int_0^f r^2(I-u_{\text{in}})dr \\ &\quad +2(\frac{\delta u_{\text{out}}}{\delta f})\int_f^{B(I)} r^2(I-u_{\text{out}})dr, \end{aligned} \tag{17}$$

and

$$\frac{\delta u_{\text{in}}}{\delta f} = \frac{\int_{S^2} f^2I(f)d\Omega_{S^2}-u_{\text{in}}\,\text{surf}(f)}{\text{vol}(\text{inside}(f))}, \tag{18}$$

$$\frac{\delta u_{\text{out}}}{\delta f} = -\frac{\int_{S^2} f^2I(f)d\Omega_{S^2}-u_{\text{out}}\,\text{surf}(f)}{\text{vol}(\text{outside}(f))}, \tag{19}$$

and $\text{surf}(f)=\int_{S^2} f^2d\Omega_{S^2}$ is the surface area of the evolving surface.

D. PDE Linearization

Comparing equation (16) with (4), it is clear that the Euler-Lagrange equation (16) is no longer a homogeneous Helmholtz PDE due to two factors: 1) g_f is non-linear in f, 2) the additive region-based penalization term z is not linear in f. The same issue was encountered in [18] and the authors circumvented the problem by implementing an iterative approach which linearizes f about the surface computed in the previous step followed by update propagation. Update propagation is a kind of successive approximation scheme for which, at iteration $n+1$, we update f_n in terms of the past iterate $f_n(\theta', \phi')$, if f_{n+1} for (θ', ϕ') has not yet been computed, and a partial update $f_{n+1}(\theta', \phi')$, if f_{n+1} for (θ', ϕ') has been computed. This succesive approximation idea can be similarly applied to (16) to transform it to of a homogeneous linear Helmholtz equation. Combining all the non-linear terms in the PDE into a single term and moving this term to the right side of the equation, (16) can be rewritten as:

$$\alpha \nabla^2 f - f = \gamma z(f, I) - (f - g_f)\frac{\partial g_f}{\partial f} - g_f. \tag{20}$$

Invoking the assumed dominance condition $|(f - g_f)\frac{\partial g_f}{\partial f})| \ll g_f$, and replacing the right hand side of (20) with the value of f_n, we obtain a linearized homogeneous Hemholtz equation

$$\alpha \nabla^2 f_{n+1} - f_{n+1} = \gamma z(f_n, I) - g_{f_n}. \tag{21}$$

This evolution equation bears some similarity to the surface evolution equations used in FDM, e.g.,

$$f_{t+\Delta t} = f_t + [\alpha \nabla^2 f_t - (f_t - g_{f_t})(1 - \frac{\partial g_{f_t}}{\partial f_t}) - \gamma z(f_t, I)]\Delta t \tag{22}$$

where Δt is the FDM time step which indexes the sequqnce of evolving surfaces.

III. Fast 3D Spectral Approach

As we have discussed in the introduction, FDM [37] and FEM [12] have been used to solve the Euler-Lagrange equations associated with active surfaces. However, all of these methods have difficulties for 3D images due to the inherently large required grid sizes. Spectral methods for solving PDE's over a 2D rectangular domain are renowned for their faster rate of convergence and higher accuracy as compared to iterative FEM and FDM. These SM approaches take advantage of symmetries by transforming the equation into the spectral domain. They only require $O(N^2 \log N)$ operations for a 2D problem on a $N \times N$ grid. It was Simchony who first applied SM to solve Poisson equations on 2D rectangles for computer vision problems [30]. Although similar methods for solving PDE's over the unit sphere have been used in numerical weather prediction and the study of ocean dynamics [9], [38], to the best of our knowledge, we are the first to propose applying them to 3D computer vision problems.

When the PDE (21) is expressed in spherical coordinates, the use of basis functions, such as spherical harmonics (SH), double Fourier series (DFS) and Chebyshev polynomials, has attractive features. An instructive comparison of these functions is given by Boyd in [4]. Due to the spherical geometry, conditions must be imposed on the basis functions to ensure that the approximated radial function f and its corresponding derivatives are continuous at the poles. For more discussions of the pole problem, readers are refered to [5]. The SH basis can easily handle this pole problem because of properties of the associated Legendre functions. However the Legendre functions also make the computation of SH representations the most computationally intensive among the three aforementioned basis sets. On the other hand, the DFS can give comparable accuracy and are more easily computed. Furthermore, use of the fast fourier transform (FFT) can accelerate the computation of DFS.

As far as we know Yee [38] was the first to apply truncated double Fourier series to solve Poisson-type equations on a sphere. However, Yee's algorithm had the deficiency of not properly enforcing continuity at the spherical poles. Recently, Cheong proposed a new method which is similar to Yee's method, but directly enforces continuity at the poles and leads to increased accuracy and stability for time-stepping PDE solution procedures [9]. In the following sections, we discuss our application of Cheong's spectral method for solving the Helmholtz equations associated with computing active surfaces. Notice that μ in Eq. (4) $\nabla^2 f - \mu(f-g) = 0$ and α in Eq. (21) $\alpha\nabla^2 f - (f - g_f)(1 - \frac{\partial g_f}{\partial f}) = 0$ can be unified by identifying $\alpha = 1/\mu$.

A. The Spectral Method

Here we briefly describe the spectral method proposed by Cheong. The elliptic equation $\nabla^2 f - \mu(f-g) = 0$ is a Helmholtz equation. The Laplacian operator ∇^2 on the unit sphere has the form:

$$\nabla^2 = \frac{1}{\sin\theta}\frac{\partial}{\partial\theta}(\sin\theta\frac{\partial}{\partial\theta}) + \frac{1}{\sin^2\theta}\frac{\partial^2}{\partial^2\phi}. \tag{23}$$

We assume the value of function f and g are given on the grid (θ_j, ϕ_k), $\theta_j = \pi(j+0.5)/J$ and $\phi_k = 2\pi k/K$, where J and K are the number of data points along the latitude and longitude angles. We can expand the function g, and similarly for f, in a truncated Fourier series in longitude with truncation index M, e.g.,

$$g(\theta,\phi) = \sum_{m=-M}^{M} g_m(\theta)e^{im\phi_k} \tag{24}$$

where $g_m(\theta)$ is the complex Fourier coefficient given by $g_m(\theta) = \frac{1}{K}\sum_{k=0}^{K-1} g(\theta,\phi_k)e^{-im\phi_k}$, $\phi_k = 2\pi k/K$ and $K = 2M$. Equation (4) can then be written as an ordinary differential equation:

$$\frac{1}{\sin\theta}\frac{d}{d\theta}\left(\sin\theta\frac{d}{d\theta}f_m(\theta)\right) - \frac{m^2}{\sin^2\theta}f_m(\theta) = \mu[f_m(\theta) - g_m(\theta)] \tag{25}$$

The latitude function $f_m(\theta)$ and $g_m(\theta)$ can be further approximated by the truncated sine or cosine functions,

$$\begin{aligned} g_m(\theta_j) &= \sum_{n=0}^{J-1} g_{n,0}\cos n\theta_j, && m = 0 \\ g_m(\theta_j) &= \sum_{n=1}^{J} g_{n,m}\sin n\theta_j, && \text{odd } m \\ g_m(\theta_j) &= \sum_{n=1}^{J} g_{n,m}\sin\theta_j\sin n\theta_j, && \text{even } m \neq 0. \end{aligned} \tag{26}$$

Equations (24)-(26) constitute Cheong's method and an efficient procedure for calculating the spectral coefficients $g_{n,m}$ can be found in [9]. After substitution of (26) into (25), we obtain an algebraic system of equations in Fourier space:

$$\begin{aligned} \frac{(n-1)(n-2)+\mu}{4}f_{n-2,m} - \frac{n^2+2m^2+\mu}{2}f_{n,m} + \frac{(n+1)(n+2)+\mu}{4}f_{n+2,m} \\ = \mu[\frac{1}{4}g_{n-2,m} - \frac{1}{2}g_{n,m} + \frac{1}{4}g_{n+2,m}], m = 0, \text{or odd} \end{aligned} \tag{27}$$

and

$$\begin{aligned} \frac{n(n-1)+\mu}{4}f_{n-2,m} - \frac{n^2+2m^2+\mu}{2}f_{n,m} + \frac{n(n+1)+\mu}{4}f_{n+2,m} \\ = \mu[\frac{1}{4}g_{n-2,m} - \frac{1}{2}g_{n,m} + \frac{1}{4}g_{n+2,m}], m \text{ even} \neq 0 \end{aligned} \tag{28}$$

where $n = 1, 3, \cdots, J-1$ for odd n, $n = 2, 4, \cdots, J$ for even n if $m \neq 0$ and $n = 0, 2, \cdots, J-2$ for even n, $n = 1, 3, \cdots, J-1$ for odd n if $m = 0$. Equations (27) and (28) imply that the components of even and odd n are uncoupled for any given m. These equations can be rewritten in matrix format,

$$\mathbf{B}\underline{f} = \mathbf{A}\underline{g} \tag{29}$$

where $\mathbf{B}$ and $\mathbf{A}$ are matrices of size $J/2 \times J/2$ with tridiagonal components only, $\underline{f}$ and $\underline{g}$ are column vectors whose components are the expansion coefficients of $f_m(\theta)$ and $g_m(\theta)$. For example, the system (29) for odd n looks like the following:

$$\begin{pmatrix} b_{1,m} & c_1 & & & \\ a_3 & b_{3,m} & c_3 & & \\ & \ddots & \ddots & \ddots & \\ & & a_{J-3} & b_{J-3,m} & c_{J-3} \\ & & & a_{J-1} & b_{J-1,m} \end{pmatrix} \begin{pmatrix} f_{1,m} \\ f_{3,m} \\ \vdots \\ f_{J-3,m} \\ f_{J-1,m} \end{pmatrix} =$$

$$\begin{pmatrix} 2 & -1 & & & \\ -1 & 2 & -1 & & \\ & \ddots & \ddots & \ddots & \\ & & -1 & 2 & -1 \\ & & & -1 & 2 \end{pmatrix} \begin{pmatrix} g_{1,m} \\ g_{3,m} \\ \vdots \\ g_{J-3,m} \\ g_{J-1,m} \end{pmatrix}$$

The procedure to solve the equation (4) can now be made explicit: First, we compute $g_{n,m}$, the spectral components of $g(\theta, \phi)$ by double Fourier series expansion. Then the right hand side of (29) is calculated to obtain the column vector $\underline{g}_1 = \mathbf{A}\underline{g}$. Finally, the tridiagonal matrix equation $\mathbf{B}\underline{f} = \underline{g}_1$ is solved and $f(\theta, \phi)$ is obtained by inverse transform of $f_{n,m}$ via formulas (24) and (26) with $g_{n,m}$ and $g(\theta, \phi)$ replaced by $f_{n,m}$ and $f(\theta, \phi)$, respectively. Notice that the Poisson equation $\nabla^2 f = g$ is just a special case of the Helmholtz equation, so that a slight modification in the above algorithm will also give the solution to homogeneous Poisson equations. Other homogeneous elliptic equations, such as biharmonic equations can also be solved by this spectral method.

Using the spectral method described above to solve the PDE (21) we propose the following evolution algorithm for implementing our fast spectral method

FSM Active Surface Algorithm

1. Initialize the evolving surface with a sphere of radius c.
2. Compute $g_{f_n}(\theta, \phi)$ and update the RHS of (21) with f_n and g_{f_n};
3. Solve the PDE $\alpha\nabla^2 f_{n+1} - f_{n+1} = \gamma z(f_n, I) - g_{f_n}$ for f_{n+1} to update the surface;
4. Compute the error, $e_{n+1} = \sqrt{\frac{\sum_{j=0}^{J-1}\sum_{k=0}^{K-1}(f_n(\theta_j,\phi_k) - f_{n+1}(\theta_j,\phi_k))^2}{JK}}$
5. If $e_{n+1} >$ threshold, go back to 2, else end.

In the above algorithm, α and γ are chosen in advance to control the tradeoff between surface fidelity to the edge map and surface smoothness.

B. Complexity and Accuracy Analysis

Consider an elliptic equation with a grid size of $N \times N$ on unit sphere. The FDM solver requires a total of N^2 variables with matrix size $N^2 \times N^2$. A crude Gauss elimination method will require $O(N^6)$ operations and the Gauss-Siedel relaxation will require $O(N^4)$ operations to converge. The number of operations might be reduced to $O(N^3)$, if the algorithms can exploit matrix sparseness. However, using the results of [9], the

computational complexity of FSM is only $O(N^2 \log N)$. The objective in this subsection is to evaluate and compare FDM, FEM and FSM PDE solvers for the one iteration of the evolving surface algorithm, i.e., for solution of the Helmholtz equation (21) on the sphere.

To compare the complexity of FSM and FEM on the sphere, we implemented a "cubed-sphere" FEM algorithm similar to that of Ronchi [27]. The method is based on a decomposition of the sphere into six identical regions, obtained by projecting the sides of a circumscribed cube onto a spherical surface. A composite mesh can then be generated for the FEM PDE solver. In Table I, we list the CPU times of FSM and FEM for solving the Helmholtz equation on the sphere $\nabla^2 f - \epsilon f = g$, where g is a random polar function and $\epsilon = 100$. In Table II, the L_2 errors of the two methods are listed for solving the Poisson equation $\nabla^2 f = g$. We choose $g = 3\sin(2\theta)\cos(\phi)$ as the force function so that the analytical solution $f = -0.5\sin(2\theta)\cos(\phi)$ can be used for accuracy analysis of the two methods. It can be seen that the spectral method is not only faster than the "cubed-sphere" FEM but also more accurate than the "cubed-sphere" FEM. These comparisons were implemented on a Sun-Blade 100 Unix machine under MATLAB.

TABLE I

CPU TIME OF SPECTRAL HELMHOLTZ SOLVERS BASED ON FSM AS COMPARED TO THE "CUBED-SPHERE" FEM SOLVER

Number of grid points		CPU time (sec)	
FSM	FEM	FSM	FEM
$16 \star 16$	$6 \star 6 \star 6$	2.0E-2	3.4E-1
$32 \star 32$	$6 \star 13 \star 13$	5.0E-2	6.4E-1
$64 \star 64$	$6 \star 26 \star 26$	1.3E-1	1.3
$128 \star 128$	$6 \star 52 \star 52$	3.8E-1	3.6

TABLE II

L_2 ERRORS FOR THE POISSON SOLVERS BY THE SPECTRAL METHOD BASED ON DOUBLE FOURIER SERIES AND THE "CUBED-SPHERE" FEM

Number of grid points		L_2 error	
FSM	FEM	FSM	FEM
$16 \star 16$	$6 \star 6 \star 6$	1.3E-2	4.9E-2
$32 \star 32$	$6 \star 13 \star 13$	5.6E-11	1.8E-2
$64 \star 64$	$6 \star 26 \star 26$	8.5E-15	9.9E-3
$128 \star 128$	$6 \star 52 \star 52$	4.5E-15	6.4E-3

To compare FSM to FDM it suffices to inspect Table III, which is derived from Shen [29]. Shen performed a numerical experiment which applied spectral methods and the FDM to solve the same Helmholtz equation on the sphere. The CPU time comparison in Table III indicates that the spectral method based on double Fourier expansion is significantly more efficient when compared with the spectral method based on spherical harmonics and the algorithm based on FDM. The experiments done by Merill in [23] gave similar results. Notice that Shen's spectral methods have runtimes that are faster than those reported for our spectral method. One possible and reasonable explanation is that his methods were implemented on different platforms using different implementation codes (Shen used Fortran while we used MATLAB).

IV. APPLICATIONS

In the Section we illustrate the FSM active surface method for simulated and real 3D image volumes.

TABLE III

CPU TIME FOR HELMHOLTZ SOLVERS ON THE SPHERE. (FROM SHEN [29])

$N = M$	32	48	64	96	128	192	256
Spherical harmonics	6.2E-3	1.7E-2	3.7E-2	.12	.28	1.19	3.06
Fourier I	6.6E-3	1.4E-2	2.3E-2	5.3E-2	9.0E-2	.24	.42
Fourier II	7.1E-3	1.5E-2	2.4E-2	6.0E-2	.11	.27	.46
FISHPACK(FDM)	6.8E-3	3.1E-2	6.9E-2	.13	.27	.65	1.22

A. Surface Reconstruction

We first performed experiments to compare reconstructions of a sphere and an ellipsoid in order to illustrate the role of the regularization parameter $\alpha = 1/\mu$. We simulated the effect of isotropic segmentation noise by adding circular Gaussian segmentation noise to the spherical harmonic coefficients. In Figure 2, the reconstruction error is plotted versus the value of μ for two shapes. The horizontal line represents the standard deviation of the segmentation noise. The figure shows that for the simple spherical shape, which only contains a single SH frequency component, the value of μ should be as small as possible in order to filter out segmentation noise, while for a shape containing higher spatial frequencies, such as the ellipsoid, μ should be optimized to control the tradeoff between denoising and matching high spatial frequencies. Note also that as the standard Euclidean norm of the gradient is adopted to enforce smoothness, a spherical surface minimizes the energy function for $\mu = 0$. When the edge map is derived from an ellipsoidal surface the optimum value of μ lies between 10^1 and 10^2. If μ is too small the evolving surface is overly attracted to the mismatched spherical shape. On the other hand, if μ is too high, the segmentation noise dominates the reconstruction. One possible method for improving accuracy is to use prior information to induce more suitable shape attractors, e.g., implementing a weighted norm on the evolving surface gradient.

The optimum value of μ not only changes with different shapes, but also with different segmentation noise levels. In our second experiment, we investigated changes in the standard deviation of the segmentation noise for an ellipsoidal shape. Figure 3 shows that μ should be smaller for low SNR segmentation data than for high SNR segmentation data, which is as expected. Three reconstructions of the ellipsoid are presented in Figure 4. As previously described, the perceived goodness of fit of the final reconstructed surfaces is determined by the value of μ.

B. 3D Parametric Active Surfaces

B.1 Active Surface with Region-based Penalization

The region-based penalization method described in Section II was applied, in conjunction with the FSM active surface algorithm, to a synthesized 3D image to show the advantage of leakage prevention. An ellipsoid is contained in a $128 \times 128 \times 64$ image. One side of the ellipsoid boundary has been blurred with a linear filter, a single slice of which is shown in Figure 5. The set of edgemaps of the blurred 3D image is shown in Figure 6 and were derived from the blurred image by the Canny edge detector implemented with the MATLAB function edge(). Both the blurred grey-level image and the set of extracted edgemaps were then used to drive our penalized active surface algorithm . Figure 7(a) shows that without region-based penalty, severe leakage of the surface occurs in the vicinity of the blurred boundary. Figure 7(b) illustrates the positive effect of region-based penalization. In this experiment, we chose $\alpha = 10^{-6}$ and $\gamma = 5\alpha$. The penalization in each direction is proportional to f^2.

B.2 Liver Shape Extraction

In this experiment, we applied the FSM active surface algorithm (without region-based penalty) to 3D human liver extraction from an actual thoracic X-ray CT scan. The X-ray CT image was obtained as a stack of 2-D image slices each of size 256×256. Double Fourier series were used to expand the radial function of a 3D sphere initialized inside the liver volume. The edge maps were again obtained by Canny filtering. The CT slices and the corresponding edgemaps are shown in Figure 8.

As in the ellipsoidal surface reconstruction experiment, the center of the liver was estimated in advance. Although it was not implemented in our experiment, dynamic center estimation could in principle be applied as the surface evolves. The surface was initialized as a sphere inside the liver. The initial radius was set to half of the distance from the origin to the edge point closest to it. A 64×64 grid was used for the 3D active surface. At the nth iteration, the closest edge map g_{f_n} is determined from f_n and g as explained in Section II-D. The elliptic equation was then solved to propagate the active surface to the new position f_{n+1}. Because the boundary information extracted by local edge detector has been integrated into the PDE, the average distance from the evolving surface to its convergent limit is within one pixel after only 5 iterations.

Figure 9 shows a slice of the final 3D surface obtained with different values of α. When $\alpha = 10^{-3}$, the surface is over regularized and overly attracted to a spherical surface by the isotropic smoothness penalty. When $\alpha = 10^{-6}$, the regularization effect is so weak that the final surface is virtually unregularized. Empirically, it appears that $\alpha = 10^{-4}$ yields the closest match to the true outline of the liver. This further emphasizes the importance of studying the effect of the regularization parameter α on final accuracy. Finally, Fig. 10(a) shows the under-regularized final active surface while (b) shows the final surface with $\alpha = 10^{-4}$.

V. Conclusions

In this paper, we have discussed the formulation of 3D surface reconstruction using spectral active surfaces with edge penalties implemented in spherical geometry. The spectral method uses double Fourier series as orthogonal basis to solve a sequence of elliptic PDE's over the unit sphere. Compared to the complexity of $O(N^3)$ for iterative time domain (FDM) balloon methods, the complexity of $O(N^2 \log N)$ for spectral methods is significantly lower. Our experiments demonstrated fast convergence of edge penalized spectral active surfaces for simulated edge maps and those derived from actual 3D thoracic CT scans. We extended the 3D spectral active surface methods to region-based penalty functions allowing the surface to account for grey-scale variations and control leakage at blurred boundaries. The choice of active surface regularization parameters requires further study. A limitation of the spectral method is that it requires a regular sampling grid and thus cannot incorporate local mesh refinement in the region of large curvatures. Another limitation is the requirement of star-shaped objects. We believe that a hybrid spectral/finite-element method that provides the advantages of each should be explored to alleviate these difficulties.

References

[1] G. Aubert and P. Kornprobst, *Mathematical problems in image processing: Partial Differential Equations and the Calculus of Variations*, Springer, 2002.

[2] L. Bers, F. John, and M. Schechiter, *Partial Differential Equations*, John Wiley and Sons, 1964.

[3] G. J. Boer and L. Steinberg, "Fourier series on sphere," *Atmosphere*, vol. 13, pp. 180, 1975.

[4] J. P. Boyd, "The choice of spectral functions on a sphere for boundary and eigenvalue problems: A comparison of Chebyshev, Fourier and associated Legendre expansions," *Monthly Weather Review*, vol. 106, pp. 1184–1191, Aug. 1978.

[5] J. P. Boyd, *Chebyshev and Fourier Spectral Methods*, Springer-Verlag, New York, 1989.

[6] C. Brechbühler, G. Gerig, and O. Kübler, "Parametrization of closed surfaces for 3-D shape description," *Computer Vision and Image Understanding*, vol. 61, no. 2, pp. 154–170, March 1995.

[7] V. Caselles and J. Morel, "Introduction to the special issue on partial differential equations and geometry-driven diffusion in image processing and analysis," *IEEE Transactions on Image Processing*, vol. 7, no. 3, pp. 269 –273, 1998.

[8] T. F. Chan and L. A. Vese, "Active contours without edges," *IEEE Trans. on Image Processing*, vol. 10, no. 2, pp. 266–277, Feb. 2001.

[9] H. Cheong, "Double Fourier series on a sphere: Applications to elliptic and vorticity equations," *Journal of Computational Physics*, vol. 157, no. 1, pp. 327–349, January 2000.
[10] L. D. Cohen, "On active contour models and balloons," *Computer Vision, Graphics, and Image Processing: Image Understanding*, vol. 53, no. 2, pp. 211–218, 1991.
[11] L. D. Cohen and I. Cohen, "A finite-element method applied to new active contour models and 3-d reconstruction from cross sections," in *Proc. 3rd Int. Conf Computer Vision*, pp. 587–591, 1990.
[12] L. D. Cohen and I. Cohen, "Finite-element methods for active contour models and balloons for 2-D and 3-D images," *IEEE Transactions on Pattern Analysis and Machine Intelligence*, vol. 15, no. 11, pp. 1131–1147, 1993.
[13] L. D. Cohen, "Avoiding local minima for deformable curves in image analysis," in *Curves and Surfaces with Applications in CAGD*, A. Le Méhauté, C. Rabut, and L. L. e. Schumaker, editors, pp. 77–84, 1997.
[14] R. Courant and D. Hilbert, *Methods of Mathematical Physics*, Interscience, 1953.
[15] D. Gottlieb and S. A. Orszag, *Numerical Analysis of Spectral Methods: Theory and Applications*, Society for Industrial and Applied Mathematics, Philadelphia, 1977.
[16] P. Haigron, G. Lefaix, X. Riot, and R. Collorec, "Application of spherical harmonics to the modelling of anatomical shapes," *Journal of Computing and Information Technology*, vol. 6, no. 4, pp. 449–461, December 1998.
[17] B. Horn and M. Brooks, *Shape From Shading*, MIT Press, Cambridge, MA, 1989.
[18] S. Jehan-Besson, M. Barlaud, and G. Aubert, "Video object segmentation using Eulerian region-based active contours," in *Proceedings Eighth IEEE International Conference on Computer Vision*, volume 1, pp. 353–60, Vancouver, BC, Canada, July 2001.
[19] M. Kass, A. Witkin, and D. Terzopoulos, "Snakes: Active contour models," *International Journal of Computer Vision*, vol. 1, no. 4, pp. 321–331, 1987.
[20] B. B. Kimia, A. R. Tannenbaum, and S. W. Zucker, "Shapes, shocks, and deformations I: The components of two-dimensional shape and the reaction-diffusion space," *International Journal of Computer Vision*, vol. 15, no. 3, pp. 189–224, 1995.
[21] S. H. Lai and B. C. Vemuri, "An o(n) iterative solution to the poisson equation in low-level vision problems," in *Proceedings of Computer Vision and Pattern Recognition 1994*, pp. 9–14, 1994.
[22] J. Li, *3D shape modeling: registration, segmentation, and reconstruction*, PhD thesis, Dept of EECS, Univ. of Michigan, Ann Arbor MI 48109-2122, January 2002.
[23] D. W. Merrill, *Finite difference and pseudospectral methods applied to the shallow water equations in spherical coordinates*, Master's thesis, The University of Colorado, 1997.
[24] D. Mumford and J. Shah, "Optimal approximation by piecewise smooth functions and associated variational problems," *Communications on pure and applied mathematics*, vol. 42, pp. 577–685, 1989.
[25] S. A. Orszag, "Fourier series on spheres," *Monthly Weather Review*, vol. 102, pp. 56–75, 1974.
[26] S. J. Osher and J. A. Sethian, "Fronts propagation with curvature dependent speed: Algorithms based on Hamilton-Jacobi formulations," *Journal of Computational Physics*, vol. 79, pp. 12–49, 1988.
[27] C. Ronchi, R. Iacono, and P. S. Paolucci, "The "cubed sphere": A new method for the solution of partial differential equations in spherical geometry," *Journal of Computational Physics*, vol. 124, pp. 93–114, 1996.
[28] J. A. Sethian, "A review of recent numerical algorithms for hypersurfaces moving with curvature-dependent speed," *Journal of Differential Geometry*, vol. 31, pp. 131–161, 1989.
[29] J. Shen, "Efficient spectral-galerkin methods iv. spherical geometries," *SIAM Journal on Scientific Computing*, vol. 20, no. 4, pp. 1438–1455, 1999.
[30] T. Simchony, R. Chellappa, and M. Shao, "Direct analytical methods for solving Poisson equations in computer vision problems," *IEEE Transactions on Pattern Analysis and Machine Intelligence*, vol. 12, no. 5, pp. 435–446, May 1990.
[31] L. H. Staib and J. S. Duncan, "Deformable fourier models for surface finding in 3d images," in *Proceedings of Vision in Biomedical Computing (VBC)*, pp. 90–94, 1992.
[32] L. H. Staib and J. S. Duncan, "Model-based deformable surface finding for medical images," *IEEE Transactions on Pattern Analysis and Machine Intelligence*, vol. 15, no. 5, pp. 1996, Oct. 1996.
[33] G. Székeley, A. Kelemen, C. Brechbühler, and G. Gerig, "Segmentation of 2-d and 3-d objects from mri volume data using constrained elastic deformations of flexible fourier contour and surface models," *Medical Image Analysis*, vol. 1, no. 1, pp. 19–34, 1996.
[34] X. Tao, J. L. Prince, and D. Christos, "Using a statistical shape model to extract sulcal curves on the outer cortex of the human brain," *IEEE Transactions on Medical Imaging*, vol. 21, no. 5, pp. 513–524, 2002.
[35] D. Terzopoulos, "Image analysis using multigrid relaxation methods," *IEEE Transactions on Pattern Analysis and Machine Intelligence*, vol. 8, pp. 129–139, March 1986.
[36] S. R. Titus, *Improved Penalized Likelihood Reconstruction of Anatomically Correlated Emission Computed Tomography Data*, PhD thesis, The Univ. of Michigan, Ann Arbor, Dec. 1996.
[37] C. Xu and J. L. Prince, "Snakes, shapes, and gradient vector flow," *IEEE Trans. on Image Processing*, vol. 7, no. 3, pp. 359–369, March 1998.
[38] S. Y. K. Yee, "Solution of Poisson's equation on a sphere by truncated double Fourier series," *Monthly Weather Review*, vol. 109, pp. 501–505, 1981.

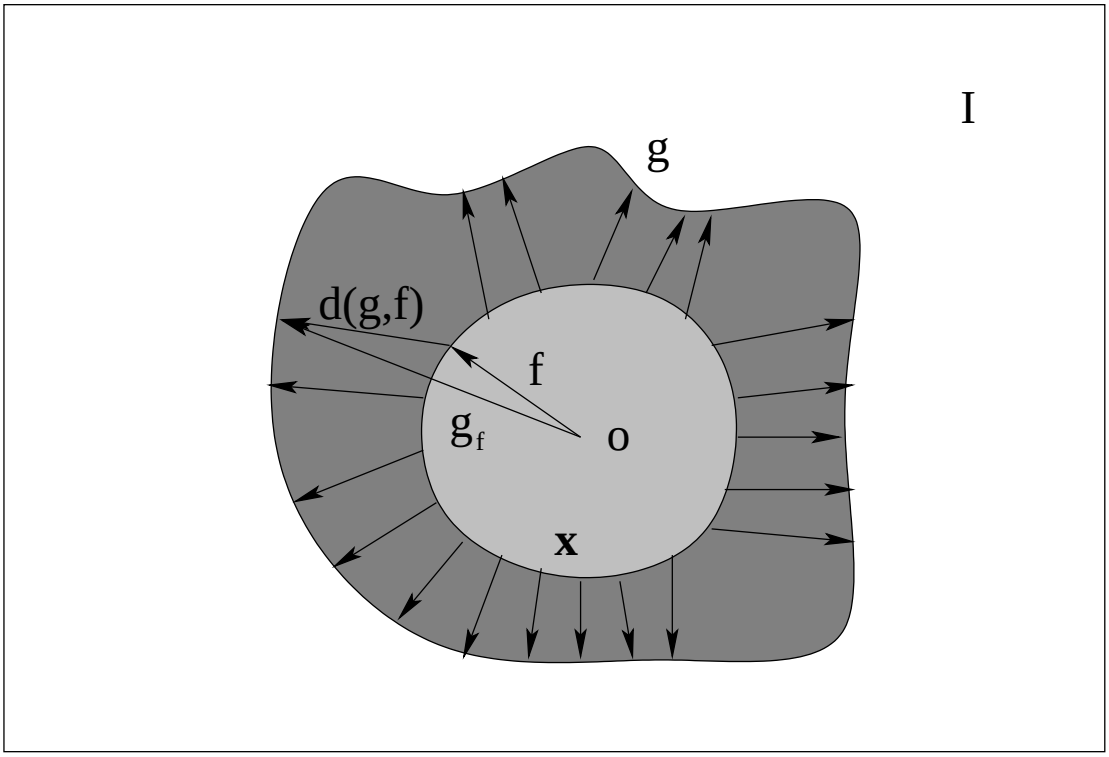

Fig. 1. A grey level image I, the set of edge points g detected in I, a propagating contour f (parameterized in polar coordinates), and the distance $d(g, f)$ between the propagating contour and its nearest edge point.

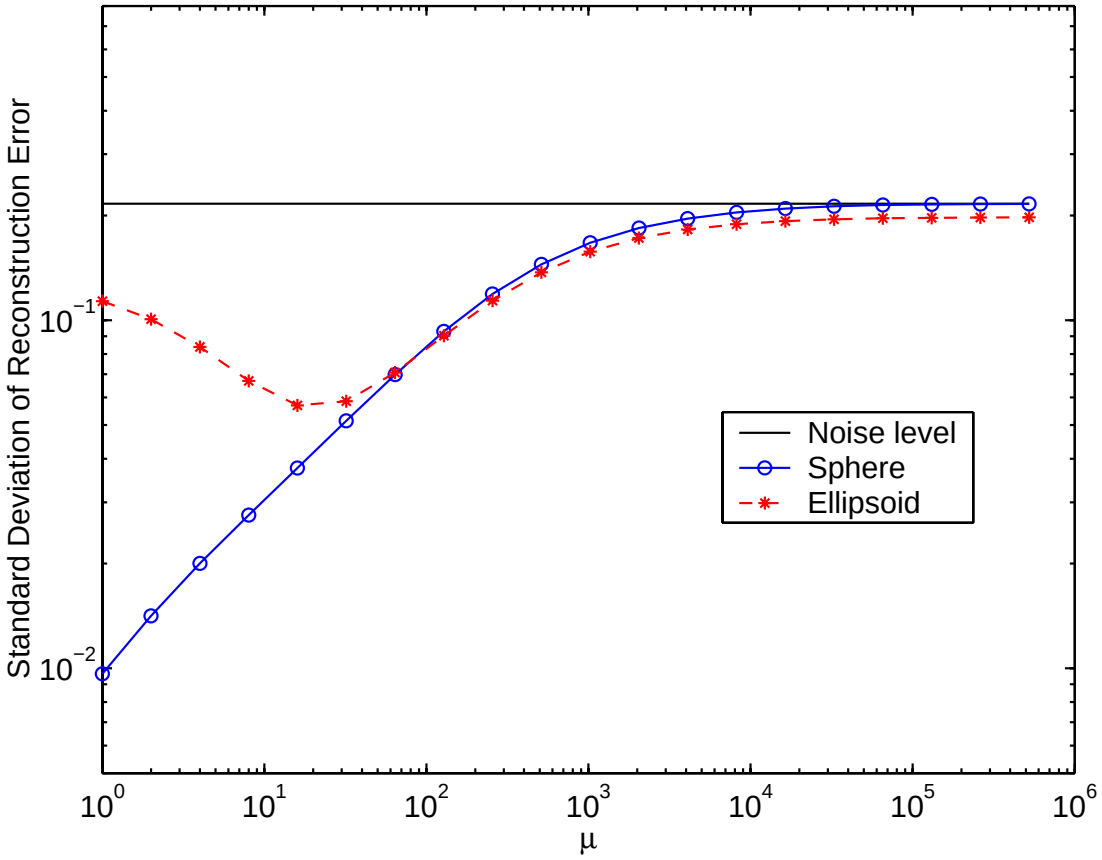

Fig. 2. Standard deviation of reconstruction error vs. regularization parameter $\alpha = 1/\mu$ for different shapes.

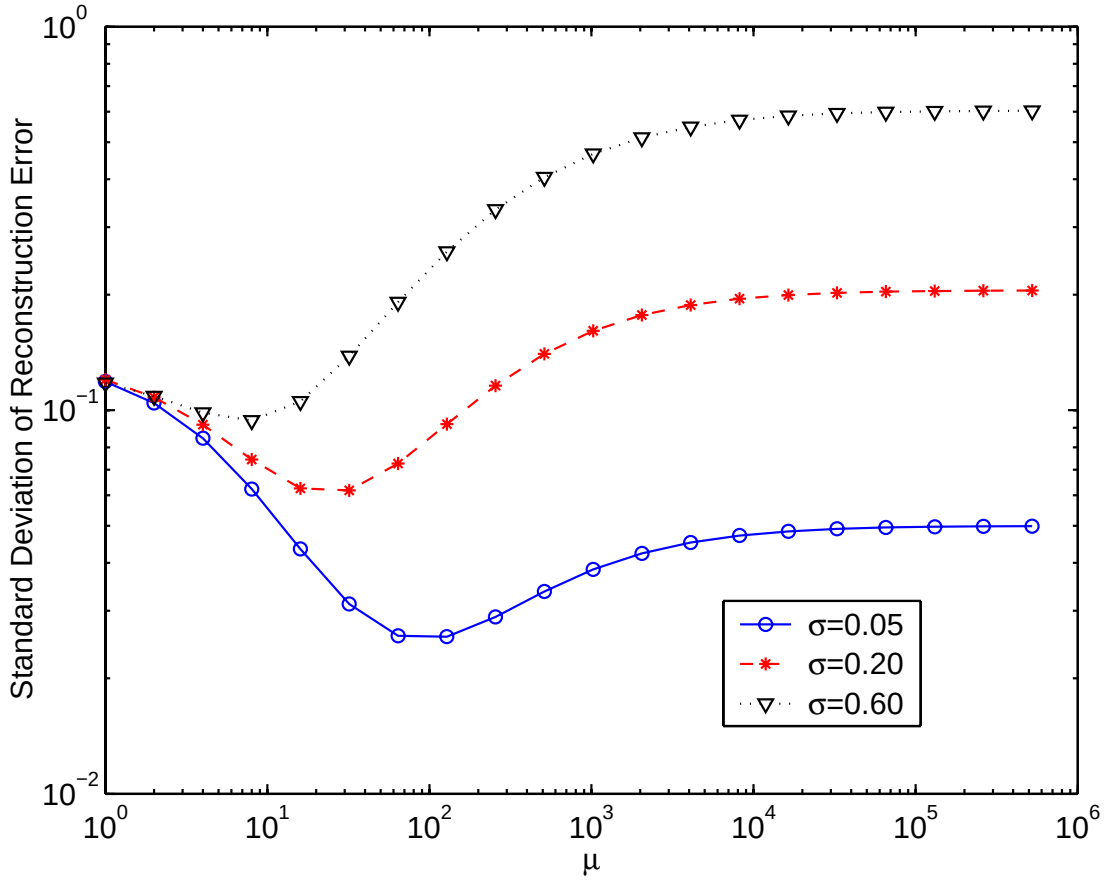

Fig. 3. Standard deviation of reconstruction error vs. regularization parameter $\alpha = 1/\mu$ for different segmentation noise levels.

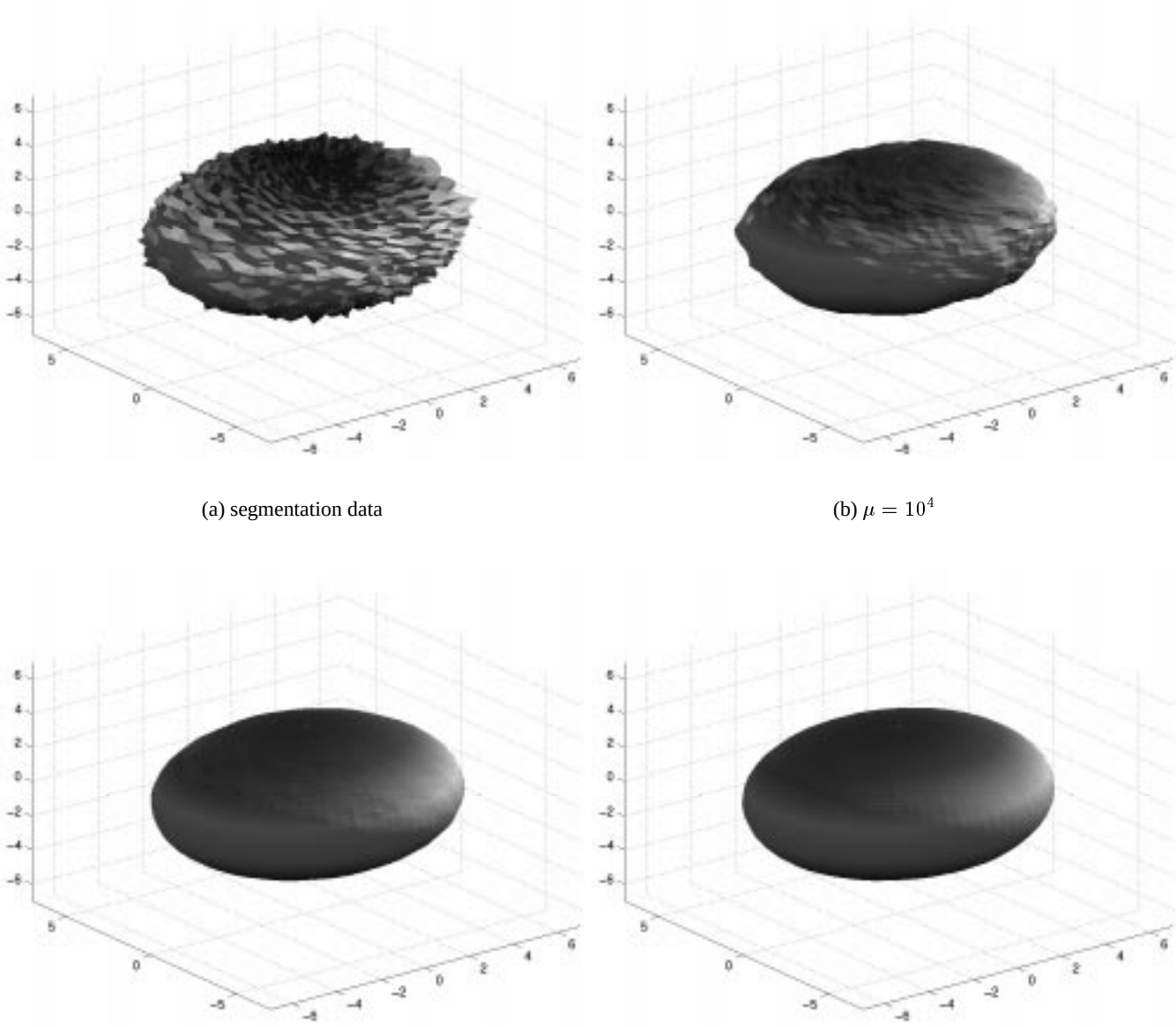

(a) segmentation data

(b) $\mu = 10^4$

(c) $\mu = 10^3$

(d) $\mu = 10^2$

Fig. 4. Final reconstruction of an ellipsoid for different values of regularization parameter $\alpha = 1/\mu$.

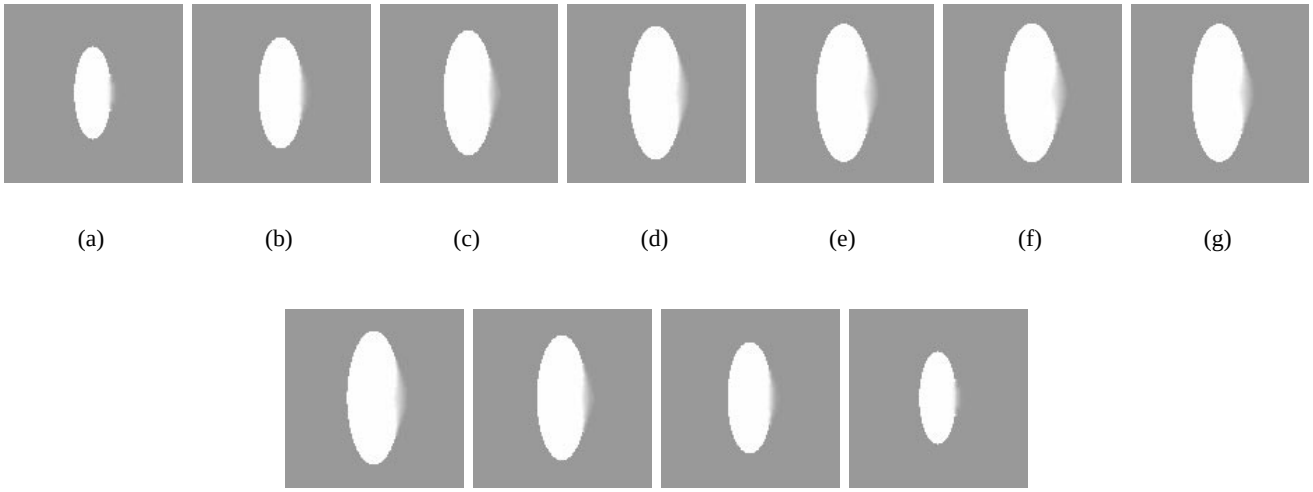

(a) (b) (c) (d) (e) (f) (g)

(h) (i) (j) (k)

Fig. 5. 2D slices of a 3D edge-blurred Ellipsoid

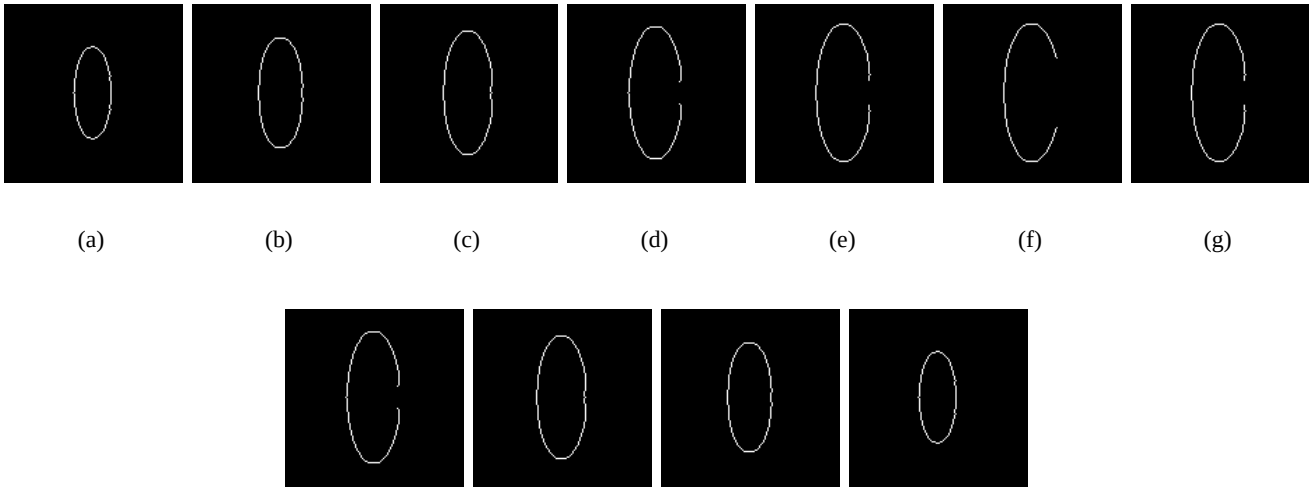

(a) (b) (c) (d) (e) (f) (g)

(h) (i) (j) (k)

Fig. 6. 2D edgemaps of the blurred 3D image containing the ellipsoid in Fig. 5.

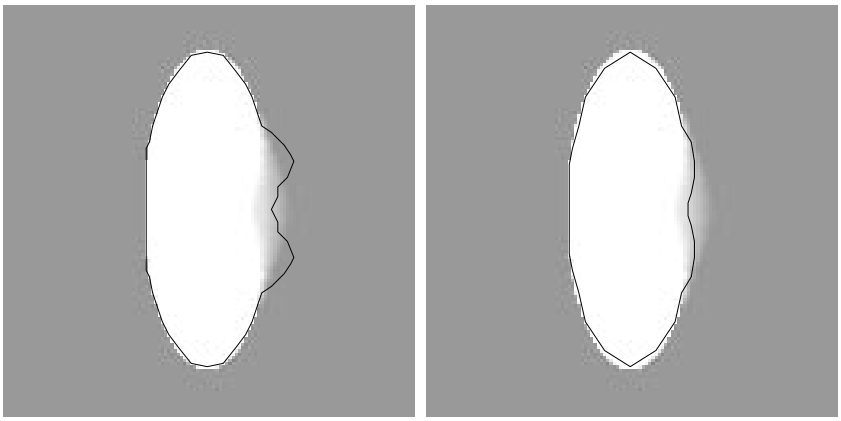

(a) No Volumetric Penalization (b) With Volumetric Penalization

Fig. 7. Segmentation comparison between FSM active surface algorithm with and without volumetric penalization for edge blurred image. Only a single slice of the full 3D segmented object is shown.

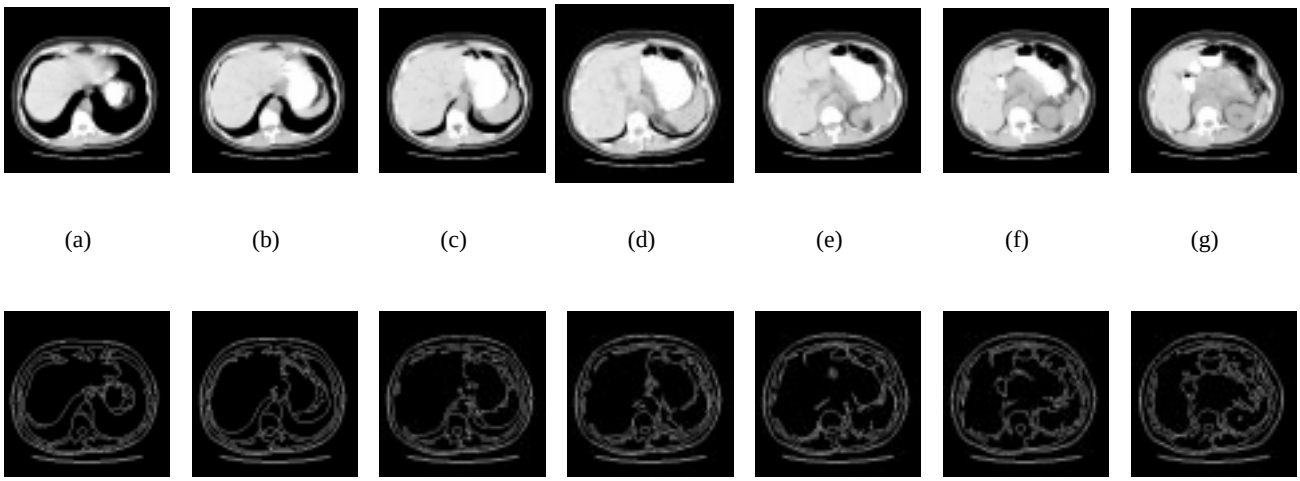

(a) (b) (c) (d) (e) (f) (g)

(h) (i) (j) (k) (l) (m) (n)

Fig. 8. CT slices of 3D thoracic image volume and the corresponding edge maps

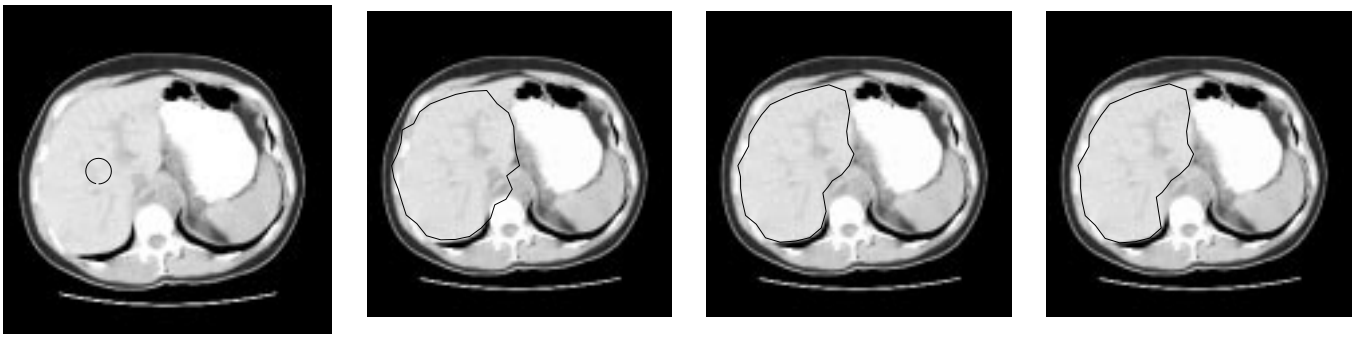

(a) Initialization (b) $\alpha = 10^{-3}$ (c) $\alpha = 10^{-4}$ (d) $\alpha = 10^{-6}$

Fig. 9. Single slice of final surface (5 iterations) of FSM active surface algorithm implemented with different values of the regularization parameter $\alpha = 1/\mu$.

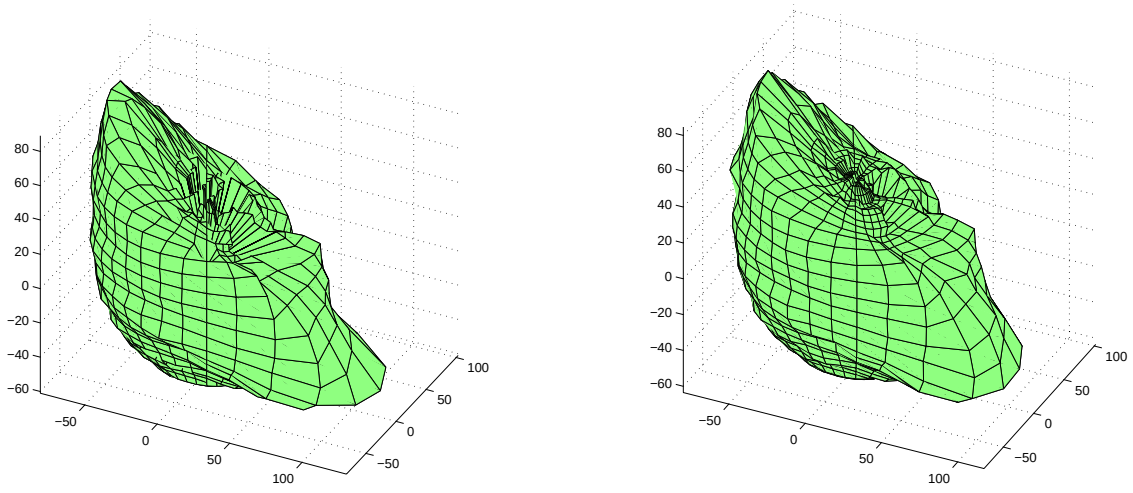

(a) Local edge detector

(b) $\alpha = 10^{-4}$

Fig. 10. Comparison of 3D shape extraction results. (a) Local edge detector without surface reconstruction; (b) result of FSM active surface reconstruction algorithm after 5 iterations with regularization parameter $\alpha = 10^{-4}$.